ADVANCED FUNCTIONAL MATERIALS
www.afm-journal.de

Check for updates

Strain-Isolating Materials and Interfacial Physics for Soft Wearable Bioelectronics and Wireless, Motion Artifact-Controlled Health Monitoring

*Nathan Rodeheaver, Robert Herbert, Yun-Soung Kim, Musa Mahmood, Hojoong Kim, Jae-Woong Jeong, and Woon-Hong Yeo**

Recent developments of micro-sensors and flexible electronics allow for the manufacturing of health monitoring devices, including electrocardiogram (ECG) detection systems for inpatient monitoring and ambulatory health diagnosis, by mounting the device on the chest. Although some commercial devices in reported articles show examples of a portable recording of ECG, they lose valuable data due to significant motion artifacts. Here, a new class of strain-isolating materials, hybrid interfacial physics, and soft material packaging for a strain-isolated, wearable soft bioelectronic system (SIS) is reported. The fundamental mechanism of sensor-embedded strain isolation is defined through a combination of analytical and computational studies and validated by dynamic experiments. Comprehensive research of hard-soft material integration and isolation mechanics provides critical design features to minimize motion artifacts that can occur during both mild and excessive daily activities. A wireless, fully integrated SIS that incorporates a breathable, perforated membrane can measure real-time, continuous physiological data, including high-quality ECG, heart rate, respiratory rate, and activities. In vivo demonstration with multiple subjects and simultaneous comparison with commercial devices captures the SIS's outstanding performance, offering real-world, continuous monitoring of the critical physiological signals with no data loss over eight consecutive hours in daily life, even with exaggerated body movements.

1. Introduction

Cardiovascular diseases affect 48% of the adult population in the United States and continue to be the number one cause of death worldwide.[1] Portable, long-term, continuous monitoring of electrocardiogram (ECG) is urgently needed to detect the onset of various arrhythmias that can happen anytime during daily activities. Many ambulatory ECG devices have been developed to provide smaller form factors than the gold-standard Holter monitor. Collecting high-quality data outside the clinical setting remains challenging due to motion artifacts. An ECG motion artifact (MA) is defined here as the temporary change in measured voltage caused by the movement of the sensor and/or body where the sensor is located. For example, walking creates a downward force on the skin and ECG device with every step, which causes temporary stretching of the skin and relative motion of the skin with the electrode. Together, these two disturbances change the half-cell potential of the skin, as well as, the contact impedance with the electrode, respectively.[2] These temporary changes in the measured voltage can have the same amplitude and frequency as the heart rate,[3] making them difficult to distinguish from many physiological signals. Although software algorithms and signal filtering are commonly used to improve signal quality, they are computationally expensive, especially for long-term monitoring, and still only provide an estimate of the actual biosignal.[4–7] Filtering can also

N. Rodeheaver, R. Herbert, Dr. Y.-S. Kim, M. Mahmood, Dr. H. Kim, Prof. W.-H. Yeo
George W. Woodruff School of Mechanical Engineering
Center for Human-Centric Interfaces and Engineering at the Institute for Electronics and Nanotechnology
Georgia Institute of Technology
Atlanta, GA 30332, USA
E-mail: whyeo@gatech.edu

Prof. J.-W. Jeong
School of Electrical Engineering
Korea Advanced Institute of Science and Technology
Daejeon 34141, Republic of Korea

Prof. W.-H. Yeo
Wallace H. Coulter Department of Biomedical Engineering
Parker H. Petit Institute for Bioengineering and Biosciences
Georgia Institute of Technology and Emory University
Atlanta, GA 30332, USA

Prof. W.-H. Yeo
Neural Engineering Center
Flexible and Wearable Electronics Advanced Research Institute for Materials
Institute for Robotics and Intelligent Machines
Georgia Institute of Technology
Atlanta, GA 30332, USA

The ORCID identification number(s) for the author(s) of this article can be found under https://doi.org/10.1002/adfm.202104070.

DOI: 10.1002/adfm.202104070

 © 2021 Wiley-VCH GmbH

be done on any signal as a secondary improvement method but is incapable of improving the raw data. Another solution is to use pressurized tight straps to restrict device movement on the skin.[8,9] However, this method causes severe discomfort and restriction of the user's activities. If a user loosens the strap pressure, the sensor loses the proper contact to the skin, resulting in signal degradation. Some devices use conductive gels to reduce impedance or strong adhesives to reduce movement, but this often creates skin rash after extended use or even skin breakdown when removed.[10–14] Recent studies have shown possible applications of dry, adhesive-free electrodes that make gentle lamination on the skin.[15–17] However, these still suffer from excessive MA caused by multiple wires, the rigidity of sensors and electronics, and the electrode's movement on the skin. Dry electrodes are especially sensitive to skin strain and vibration induced by body motion while walking, reaching, and performing other daily activities.[4,18–20] One improvement in dry electrode design was the development of thin-film, open-mesh electrodes capable of stretching with the skin. Previous works have shown some reduction of MA using the mesh electrodes compared to rigid electrodes due to their conformal contact.[21–25] Others have shown the correlation between signal quality and electrode contact area.[25–27] This led us to focus on the mechanisms causing changes to conformal contact and electrode contact area, showing that skin strain at the electrode is the main source of MA for dry electrodes. Although recently reported devices have used soft materials[28–32] or serpentine patterns,[33–35] no prior work has shown the capability of a wearable device to reduce MA caused by skin-electrode strain from external sources significantly.

This paper presents a fully-integrated, wireless, long-term usable system (soft bioelectronic system (SIS)) that physically restricts MA during multi-hour, real-life activities. Unlike the conventional sensors and systems with aggressive adhesives or straps, the presented system uses a breathable soft membrane's natural adhesion to offer a skin-friendly, comfortable, continuous recording of multiple biopotentials on the skin. We report an overview of the key materials, mechanical designs, soft packaging strategies, along with the details of the strain mechanics at the skin-electrode interface. In addition, we discuss the strain-isolation design parameters needed for the device to maintain conformal contact to the skin while simultaneously shielding the electrode from excessive skin strain and vibration during patient movement. A set of computational and experimental studies validate the mechanical reliability of the flexible and stretchable device. Signal processing workflow is outlined and demonstrated to describe the details of the monitoring of ECG, heart rate (HR), respiratory rate (RR), and activity classification. The SIS is simultaneously tested alongside two commercially available wireless devices to show the MA reduction during various physical activities in daily life. Finally, the device is worn by multiple participants for over 8 h, all performing various daily activities ranging from deskwork to exercise. As summarized in **Table 1**, compared to existing systems, the soft wearable SIS clearly shows the outstanding performance of high-quality, continuous, wireless detection of multiple physiological data with no issue of MA-based data loss.

2. Results and Discussion

2.1. Overview of Design, Fabrication, and Architecture of Strain-Isolated Soft Bioelectronics System

Figure 1 summarizes the design overview of an SIS, structure layouts, strain-isolation mechanics, and the device functions. The all-in-one, soft, imperceptible system has an exceptionally small form factor (Figure 1A) that adheres securely and discretely to the chest area for continuous health and motion monitoring throughout various daily activities. The schematic illustration in Figure 1B shows the multi-layered device structure, including a pair of skin-mounted sensors, strain-isolating blocks, soft elastomeric membranes, printed circuit board (PCB), and integrated chip components. A systematic experimental study that

Table 1. Comparison of wearable ECG monitoring systems.

Ref.	Device name (Year)	Strain reduction from sensors	Continuous data transmission	Level of activities	Substrate	Electrode type	Electrode reusability
This work	SIS (2021)	Yes (strain isolator)	>8 h[a)] (single device)	Real-time, continuous daily activities, including excessive jogging	Perforated, breathable silicone	Dry	Yes
[9]	MAX-ECG (commercial)	No	48 h[b)] (with a battery replacement)	–	Adhesive patch	Wet	No
[39]	Zio (commercial)	No	No[c)]	–	Adhesive patch	Wet	No
[11]	CAM (commercial)	No	No[c)]	–	Adhesive patch	Wet	No
[12]	Cardiostat (commercial)	No	No[c)]	–	Gel electrode	Wet	No
[40]	No name (2019)	No	<1 h (not portable)	In-lab activities	Acrylic adhesive	Wet	No
[8]	No name (2019)	No	<1 h (with a chest strap)	In-lab activities	Elastic strap	Wet	No
[31]	No name (2019)	No	3 h	Simulated in-lab sitting/standing	Silicone elastomer	Dry	Yes
[35]	SEP (2019)	No	<1 h (with a wired circuit)	Simulated in-lab jogging	Silicone elastomer	Dry	Yes

[a)]Sample rate: 256 Hz; [b)]Sample rate: 128 Hz; [c)]Data are saved to local storage, not for real-time, continuous data transmission.

© 2021 Wiley-VCH GmbH

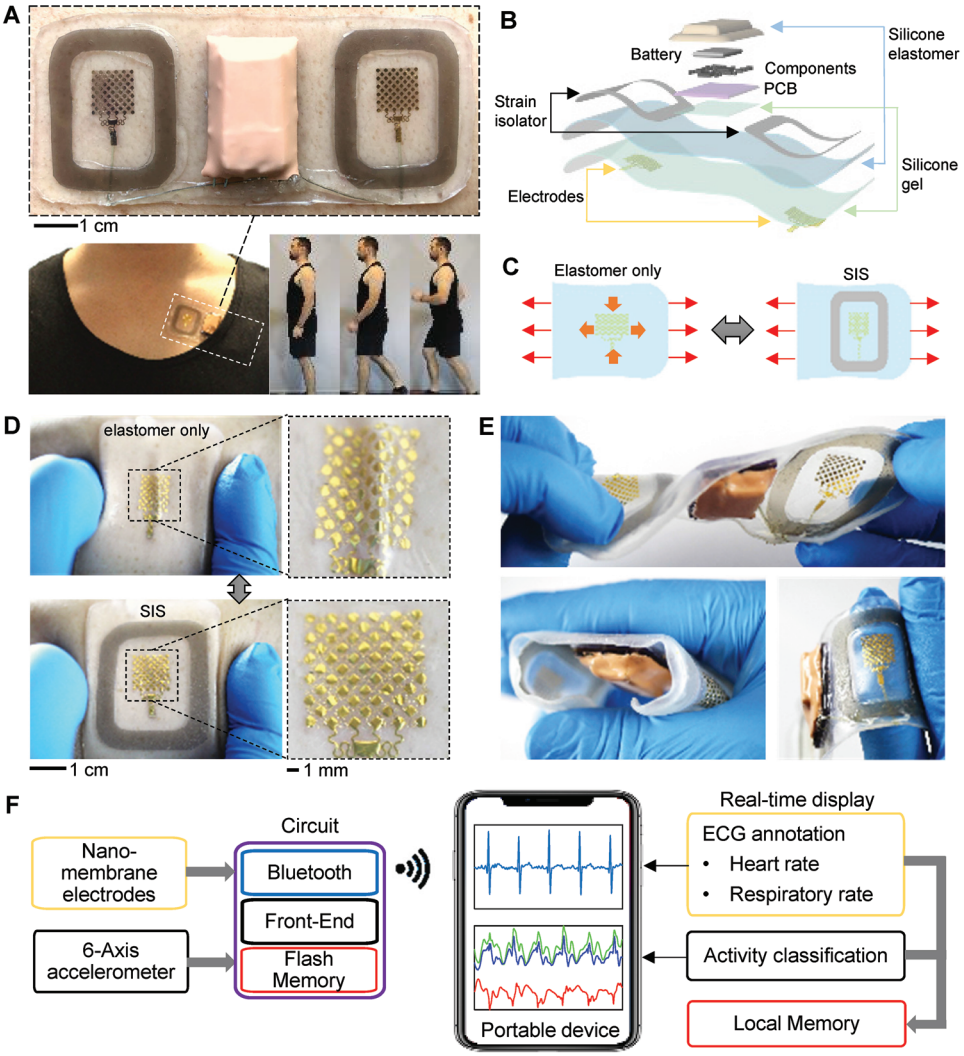

Figure 1. Overview of design, fabrication, and architecture of strain-isolated soft bioelectronics (SIS). A) Photos showing a wireless wearable soft bioelectronic system on the chest, which maintains secured contact to the skin throughout various daily activities while recording high-quality physiological signals. B) Schematic view of the multi-layered device structure, including skin-contact electrodes, soft substrates, strain isolators, chip components, and encapsulants. C) Illustration showing an electrode without a strain isolator experiencing tension and compression from uniaxial strain (left) and an electrode with negligible disturbance due to SIS (right). D) Photos that capture a nanomembrane electrode with out-of-plane buckling under external compression (top) and the same electrode with SIS that prevents buckling or sliding (bottom). E) A series of images representing the device's flexibility and small form factor. F) Schematic illustration describing the data processing workflow and signal monitoring/storage via a portable smart device.

measured skin-electrode impedance (Figure S1, Supporting Information) identified the primary source of MA to the wearable device. Among three candidates (sensor connecting wires, skin-mounted electrode, and neighboring skin), the measured impedance experienced the most significant disturbance from the applied strain to the electrode. Thus, the SIS's most crucial component is a pair of strain-isolators (SIL) in Figure 1B. The SIL is positioned above each electrode. The details of the entire device fabrication and assembly appear in Section S1 and Figure S2, Supporting Information. Among the components, a pair of nanomembrane mesh electrodes makes direct contact with the skin for measuring non-invasive physiological signals, such as ECG, HR, and RR (fabrication steps in Figure S3, Supporting Information). This open-mesh, stretchable electrode can endure excessive tensile strain up to 100% without failure (Figure S4, Supporting Information). The SIS's bottom layer is an extremely low modulus silicone gel ($E = 5$ kPa) with excellent adhesive properties to bond the device to the skin. The top layer is a low modulus silicone elastomer ($E = 68.9$ kPa) that provides a durable platform to mount the circuit and makes the device more comfortable to handle, and prevents unwanted sticking to clothes. The miniaturized PCB and rechargeable lithium-ion battery (3.7 V, 110 mAh) are secured and encapsulated with the silicone elastomer. Recharging between recording sessions is achieved by magnetic connections that protrude through the elastomer from the PCB base. The circuit is mounted in the center on a thin layer of silicone gel to allow a greater range of bending without skin delamination.

The unique feature of this design is the SIL mounted above each electrode. Figure 1C visualizes the deformation the

© 2021 Wiley-VCH GmbH

substrate and electrodes would exhibit under uniaxial strain. Typically, MA to the wearable device on the chest area arises from typical daily activities, such as standing, walking, running, or sudden arm movements. In various movement conditions, the SIL in the SIS device surrounds and shields the electrodes from excessive or sudden strain while leaving the elastomer directly over the electrodes free to maintain conformal contact at the skin-electrode interface. Photos in Figure 1D capture how the SIL can offer strain isolation for the electrode, directing skin strain to areas less critical to signal quality. Additional photos of the SIL resisting tension are provided in Figure S5, Supporting Information. Real-time recorded video clips in Videos S1 and S2, Supporting Information, clearly demonstrate the efficacy of the SIL-based strain isolation from the applied strain wave and arm movement. The entire device, including all necessary components and a rechargeable battery, still maintains mechanical flexibility and stretchability. As shown in Figure 1E, the SIS is capable of twisting, bending, and stretching, beyond the expected deformation of intended application sites on the upper torso. The schematic illustration in Figure 1F describes the data processing workflow of the SIS and signal monitoring/storage via a portable smart device. The measured data from the electrodes and the onboard accelerometer are transmitted via Bluetooth to the user's smartphone or tablet for real-time display or recording of physiological signals (details of the circuit design in Figure S6, Supporting Information). A custom-designed Android application (Figure S7, Supporting Information) can display real-time ECG data, 3-axis angular orientation data, and 3-axis acceleration. Further ECG annotation and long-term health data can be calculated at the end of each session. This is a continuation of our previous efforts to record high-quality physiological data with a skin-friendly device.[15,23,30,36] While some device designs presented by other groups aim to reduce strain at the electrodes using stiff adhesive patches or fabric backings,[8,9] they result in increased stiffness and rigidity of the device, losing the conformal electrode contact to the skin as well as consistent signal quality. On the other hand, the presented SIS maintains the quality of skin-electrode contact with a soft elastomeric membrane, while limiting the excessive strain transmission to the electrode via the SIL integration. Thus, the SIS can offer continuous, high-quality health monitoring in real-life activities at homes or clinical settings.

2.2. Strain-Isolation Method and Performance Validation of an Soft Bioelectronic System

The study summarized in **Figure 2** captures the fundamentals of strain-isolation physics via analytical calculation and computational modeling. An illustration in Figure 2A shows a section of skin and a single circular electrode subjected to biaxial strain. The shaded portion (exaggerated for emphasis) represents the human skin previously in contact with the electrode before stretching. It can be shown that the areal change (δA) is directly proportional to the local strain at the electrode. The strain defines the stretch ratios (λ_1, λ_2) which are calculated from the final dimensions (a, b) and the electrode radius (r). This is true for electrodes of any size; therefore, even mesh electrodes that stretch with the skin are still subject to a disturbance proportional to the strain at each mesh pad. The goal of the SIL is to physically prevent the temporary changes in contact impedance caused by skin strain and electrode movement or sliding. Additional notes in Section 4 and Figure S8, Supporting Information, provide a detailed definition of the stretch ratios and the proportional relationship between the strain and change in the area. The collected data in Figure 2B show the finite element analysis (FEA) result of a device with the applied tensile strain (15%) in the vertical direction to mimic a stretched human skin. The bottom electrode, without the integrated SIL, experiences 36% strain, while the top electrode that is shielded by the SIL has a calculated strain of 3%. The change in contact area for each electrode is proportional to strain, meaning that the total area of skin sliding past each tiny electrode pad on the bottom electrode is over 12 times the change occurring in the top electrode. It is clear from Figure 2B that less change occurs with the top electrode protected by the SIL. The SIL must be rigid enough to resist in-plane strain while should be flexible enough to bend out-of-plane for conformal lamination to the non-flat human skin. In this study, we used a sheet of polypropylene to fabricate the SIL. The Young's modulus (E) of the strain isolator was measured using a bending test ($E = 1.22$ GPa; Figure S9, Supporting Information). To maintain a small form factor, the length and width dimensions of the SIL were predetermined by the geometry of the electrodes and the overall device size. In the optimization study, we controlled the SIL thickness to meet both strain resistance and flexibility (Figure S10, Supporting Information). A graph in Figure 2C shows the adhesion test results from two sample thicknesses versus the bending radius for each trial. The blue area in the plot is bounded on top by the analytical calculation for the adhesion energy of the elastomer. The result determines that the allowable maximum SIL thickness is about 0.3 mm, capable of maintaining adhesion while being bent around a radius of 15 mm. The minimum thickness that is still capable of reducing strain at the electrode is about 14 µm. Details of the equations, calculation parameters, and boundary conditions appear in Section 4, and the used experimental setup for the adhesion data acquisition is shown in Figure S11, Supporting Information. Figure 2D shows additional FEA results for principal strain and Von Mises stress of the maximum and minimum SIL thicknesses. The top row with a 0.3 mm-thick SIL shows 3% strain at the electrode and stress of 4.9 MPa within the SIL. The bottom row with a 14 µm-thick SIL shows an increased strain of 21% at the electrode, and internal stress of 58 MPa; it is higher than the yield strength of the material, resulting in partial plastic deformation (details of the FEA modeling results in Figure S12, Supporting Information). Thus, we chose 0.3 mm-thick SIL to build an SIS in this study. To evaluate the performance of the SIL, short and repeatable comparison tests were conducted with a stopwatch on an indoor course. Each 3-min trial consisted of 30-s intervals for each activity in the following order: Idle (0 mph), walking (2 mph), fast walking (4 mph), jogging (6 mph), walking (2 mph), and idle (0 mph). The same device was used for eight total trials, four of which occurred before the SIL was mounted to a bare elastomer substrate, and four trials were conducted with the SIL-integrated device.

© 2021 Wiley-VCH GmbH

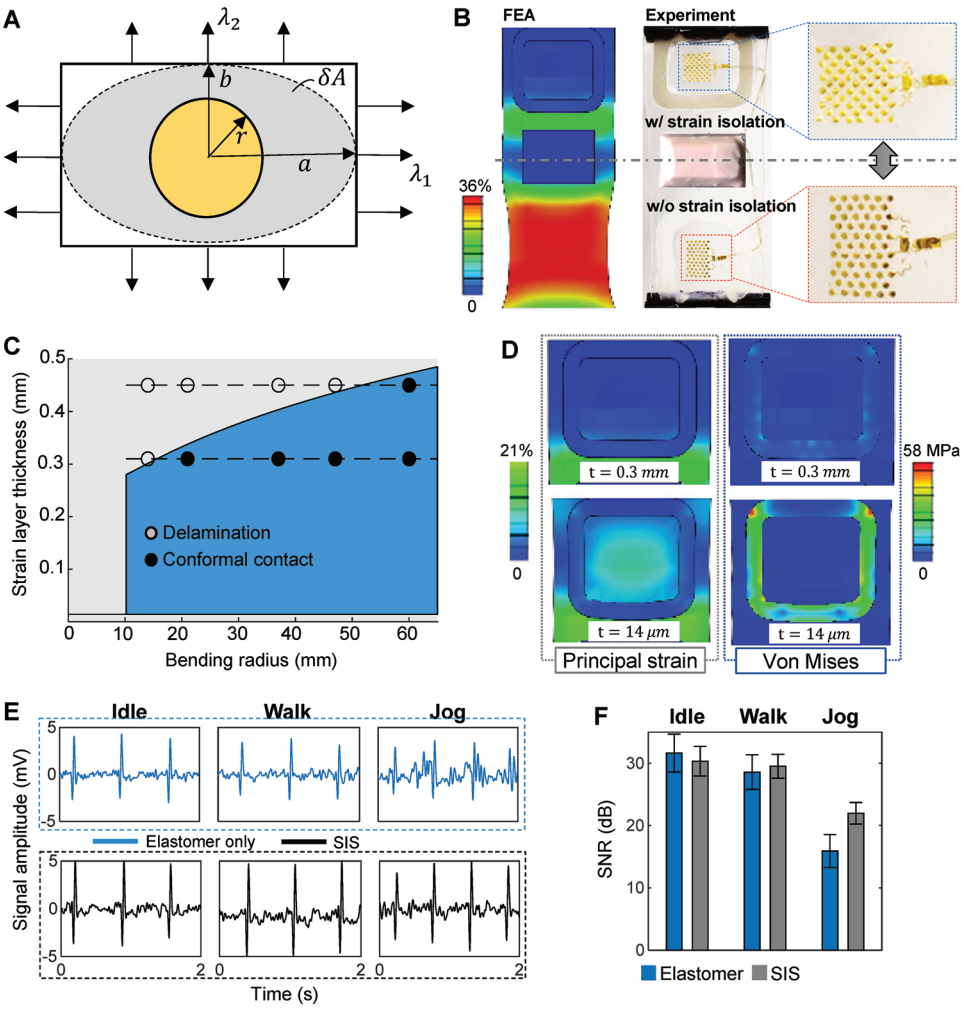

Figure 2. Details of a strain-isolation method and the performance validation of an SIS. A) Illustration of a skin-electrode model in biaxial strain with stretching ratios λ_1 and λ_2.The gold circle represents a nanomembrane sensor, while the shaded ellipse shows the skin in contact with the electrode. B) Comparison between computational finite element analysis (FEA; left) and experimental observation (right). For both cases, the top portion of the device has a strain isolator, while the bottom section shows a bare electrode on a soft membrane. Both studies show that the strain isolation layer could help maintain the sensor's shape on the skin. C) Analytical study results showing the required strain layer thickness to allow conformal contact of a sensor to the skin under varying bending radii. D) FEA results comparing the calculated principal strain and Von Mises stress between two examples—one for the 0.3 mm-thick strain layer and the other for the 14-µm thick layer. E) Comparison of measured ECG data from a sensor with a soft elastomer only (top blue graphs) and a sensor with the SIS (bottom graphs), demonstrating the motion artifact reduction during excessive movements. F) Calculated average SNR from the measured data in (E). Error bars show standard deviation ($n = 4$ trials)

Consistent skin preparation and device placement were carefully repeated, and the device was removed after each trial to demonstrate the electrode's reusability. The summarized results from Figure 2E show representative data; an SIS shows a clear reduction of MA compared to a bare elastomer case without the SIL material. The corresponding data are shown in Figure 2F where the signal to noise ratio (SNR) is calculated from all trials. Although both cases show decreased SNR during jogging, the SIS maintains better signal quality than the elastomer-only case. The mean SNR reduction from idle to jog was 31.6 to 16.9 dB for elastomer compared to 30.3 to 22.0 dB for the SIL; this is a reduction of signal quality by 47% for elastomer alone versus 27% for the SIS when compared to their respective baseline idle signals.

2.3. Signal Processing and Classification Methods for Physiological Data Analysis

The presented system, SIS, could measure non-invasive electrophysiological signals using a pair of electrodes, a 3-axis accelerator, and a 3-axis gyroscope. A flowchart in **Figure 3A** illustrates the signal processing steps used to extract ECG annotation, HR data, RR data, and activity classification. A set of graphs in Figure 3B shows actual examples (from top to bottom) of HR peak finding, RR peak detection, HR and RR moving average, and accelerometer data with activity labels (idle, walk, fast walk, and jog) for a 3-min testing routine. The raw ECG signal is initially filtered using a 0.5–30 Hz bandpass filter to remove low-frequency baseline wander and higher frequency noise, such

© 2021 Wiley-VCH GmbH

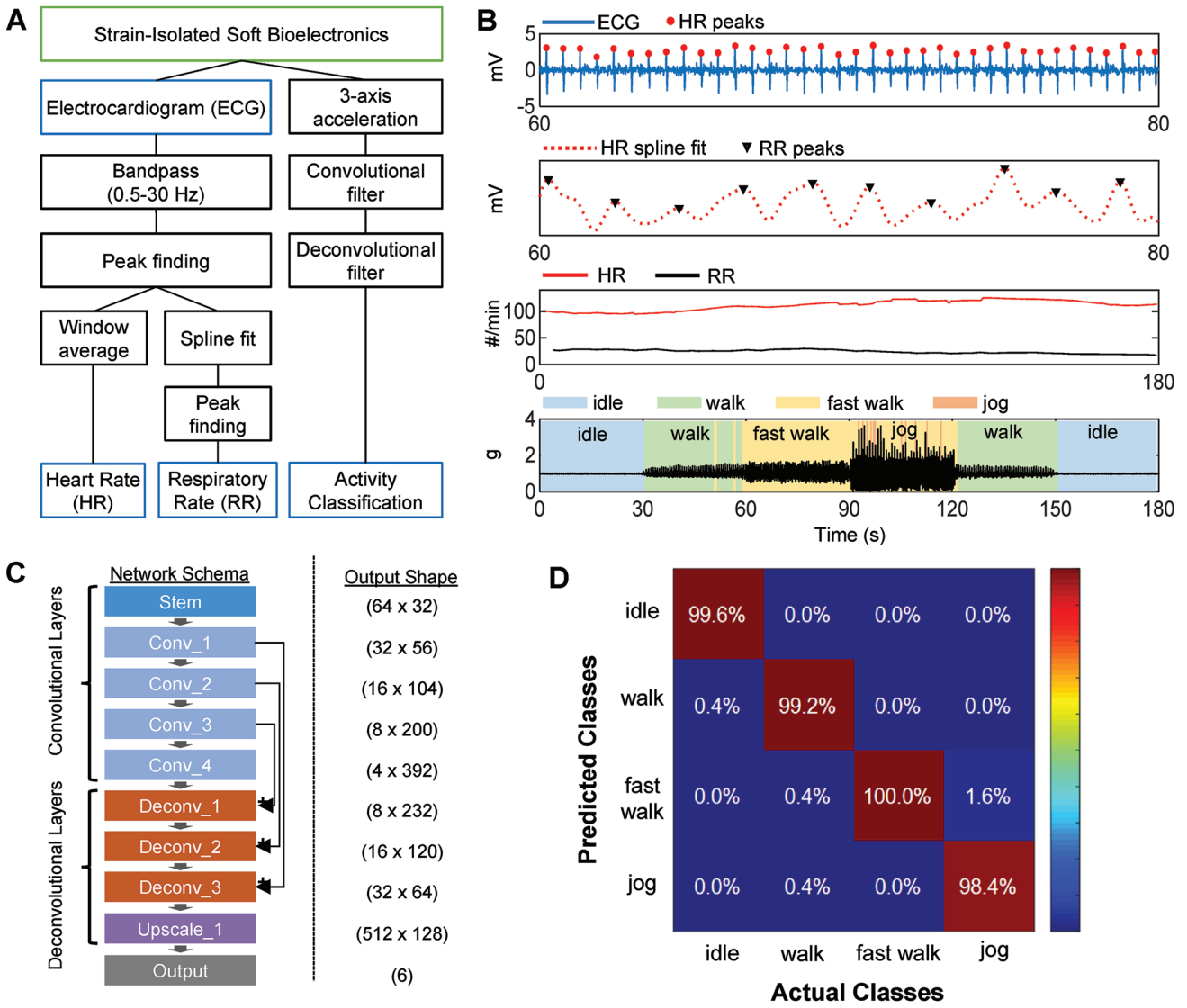

Figure 3. Signal processing and classification of physiological data. A) Signal processing flowchart of ECG and acceleration data and extraction of HR, RR, and activity scoring. B) Demonstration of an ECG annotation algorithm—HR peak detection (top), HR spline fit and RR peak counting (below), moving average data of HR and RR (below), and summarized total acceleration data with corresponding activity classification (bottom). C) Representation of CNN classification of measured acceleration data. D) A confusion matrix representing results from the real-time activity recognition, showing an overall accuracy of 99.3%.

as, chest muscle activities caused by arm motions. Next, a peak-finding algorithm identifies local maximum data points, known as the ECG waveform's R-peaks, shown as red dots in the first graph of Figure 3B. The HR is averaged using a 10-s window. Simultaneously, the HR peaks are connected using cubic spline interpolation. This new waveform, shown as the dashed red line, results from the cyclic expanding and contracting of the chest during respiration which causes the electrodes to move farther apart from each other and farther from the heart with each inhalation. This subtle change in R-peak amplitude is processed with a separate peak-finding algorithm to identify RR peaks (black triangles in the 2nd graph; Figure 3B), which are averaged using a 30-s window. The HR and RR moving averages are displayed for the entire 3-min testing routine with units of beats-per-minute and respirations-per-minute, respectively. Separately the accelerometer data is processed to categorize activity levels (bottom graph in Figure 3B). The three-axis linear acceleration is used to calculate the total linear acceleration, shown as a black line, using

$$a_{\text{total}} = \sqrt{a_x^2 + a_y^2 + a_z^2} \tag{1}$$

which provides a consistent measurement of body motion that is independent of device orientation. A machine-learning algorithm based on the residual convolutional neural network (CNN) classifies the user's activities, displayed as a color-coded background (bottom graph in Figure 3B). Total time for each category can help track daily activity. The high-level CNN

© 2021 Wiley-VCH GmbH

layers are shown in Figure 3C for the classification of 6-axis accelerometer/gyroscope data. Twelve recorded data sets were used to train the model, giving an overall accuracy of 99.3% to recognize the real-time activities of a user (Figure 3D). A detailed model with necessary layer components, residual connections, and training test process appears in Figure S13, Supporting Information. Overall, the all-in-one SIS could successfully measure multiple health-related data by simply using a user's smartphone. Primary data available in real-time, such as, average HR or activity score, can help a patient or athlete evaluate daily health conditions. Beyond that, access to the raw data enables healthcare providers to learn much more about the patient's physiological state through deeper analysis performed after the recording session has ended. The CNN activity classification was trained using data from one participant, giving a reference point that can be used to classify data from any participant guaranteeing a baseline score for each activity. Still, this model can be retrained to fit individual movement patterns or desired fitness goals. Another advantage of the chest-mounted SIS is in more accurate ECG, HR, RR, and activity detection than the existing wrist-wearable commercial health monitors.

2.4. Performance Validation of the Soft Bioelectronic System Compared to Commercial Devices

To validate the device performance, we utilized two commercial wireless heart monitors via simultaneous ECG recording on the chest area. Photos in **Figure 4A** show an SIS and a commercial all-in-one device (MAX-ECG Monitor, Maxim Integrated, Inc.) on the chest. Although both devices have a similar footprint, the commercial one contains a stiffer fabric-backed adhesive gel electrode patch shown to buckle and delaminate from the skin. The strain experienced across the entire length of the patch becomes concentrated at the edge where the circuit is connected, resulting in delamination directly over the electrode. This observation highlights the SIS's advantage of tuned stiffness specifically at the electrode, while still allowing the rest of the device to have conformal contact to the skin that can endure body movements. Figure 4B plots the SNR results from four simultaneous tests of the two devices, with mean idle values normalized for comparison. The mean SNR reduction from idle to jog was 25.7 to 12.1 dB for the commercial device compared to 25.7 to 21.6 dB for the SIS. This is a reduction of signal quality by 53% for the commercial device versus 16% for the SIS when compared to their respective baseline idle signals. Raw ECG plots in Figure 4C show 2-s comparisons for idle, walk, and jog from one trial, capturing increased MA as a user's activity level increases. On the other hand, the SIS could maintain the signal quality levels. The normalized ECG amplitudes are shown for equal comparison to compensate for the smaller signal in the commercial device partially due to its placement higher on the chest, and thereby, farther from the heart. A more extended trial with additional exercises is shown in Figure 4D. The moving average HR calculations show a slight increase during walking and jogging (30–150 s), followed by a slight decrease during resting (150–200 s) before rising higher for the remaining exercises (200–350 s). Both devices plot a similar trend throughout the test until the burpee exercise (300 s) introduces over 5-g acceleration. The SIS shows a noticeable jagged deviation indicating MA interfering with the HR algorithm, but the plot continues smoothly after the exercise is finished. Unlike the SIS, the amplitude of MA from the commercial one significantly interferes with the HR algorithm, resulting in a complete failure in HR and RR detection after 300 s (Figure 4D). Throughout the testing session, the commercial device has a higher fluctuation in detecting continuous HR and RR than the SIS. In a similar way, we compared the effect of arm movements on wearable devices. Plots in Figure 4E summarize the measured ECG data from the SIS and the MAX-ECG when a subject has constant arm movements, capturing significant MA from the commercial device. In addition, another commercial wireless device with gel electrodes (BioRadio, Great Lakes NeuroTechnologies) was used to compare the performance with the SIS. A set of experimental tests in Figure S14, Supporting Information, compares measured ECG signal quality between the SIS and two commercial devices (BioRadio and MAX). As described by prior articles,[23,30,36] the BioRadio with hanging wires and gel electrodes shows a significant reduction of SNR and more fluctuation and MA vulnerability. Real-time recorded video clips in Videos S3 and S4, Supporting Information, clearly demonstrate the efficacy of the SIS in reducing MA compared to the commercial device (MAX-ECG). Additional details of the experimental setup and measured ECG and activity data appear in Figures S15 and S16, Supporting Information.

2.5. Demonstration of an Soft Bioelectronic System Measuring Physiological Signals during Real-Life Activities

Further testing was conducted to evaluate an SIS's long-term performance for everyday use and real-life activities. The testing protocol involved normal daily activities such as, rest, deskwork, household chores, and exercises (**Figure 5A**). Participants were instructed to wear the device under comfortable clothes and follow a schedule that included activities from each category. A representative set of recorded data in Figure 5B shows an example of real-time, continuous recording of physiological data for consecutive 8 h: Raw ECG data with user-reported activities of four different colors (top), measured HR and RR data from ECG, showing clear signals even with excessive motions (middle), and acceleration data with machine learning-enabled classification of four types of activities (idle, walk, fast walk, and jog). HR and RR are continuously monitored throughout the day and activity classification without any MA issues or device delamination problems. A comparison plot in Figure 5C shows the percentage of time spent in four types of activities. It compares the reported time by a participant with the calculated time measured by the CNN activity classification. There are apparent discrepancies in the reported times by the user report and classified one. In general, participants underestimated time spent in the two lowest activity categories while overestimated time spent in the two higher activity categories. Our machine-learning algorithm could detect types of activities, as well as, exact time spent performing each category. Considering long-term continuous physiological monitoring on the skin, it is essential to maintain the quality of skin-electrode

© 2021 Wiley-VCH GmbH

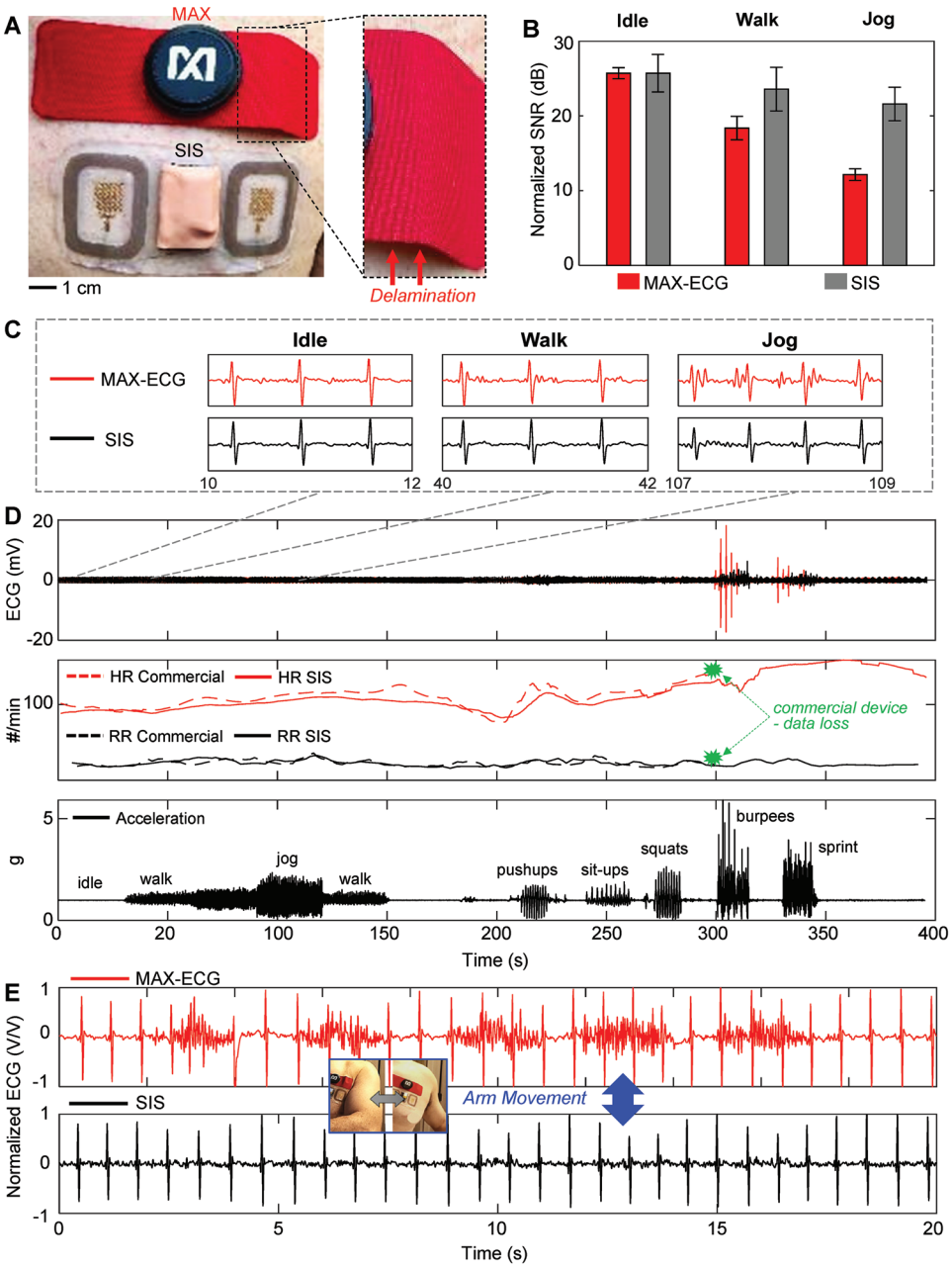

Figure 4. Performance validation of the SIS compared to a commercial device. A) Photos of two devices (commercial wearable sensor and SIS) mounted on the chest for simultaneous data recording and performance comparison. Inset shows the commercial device having a delamination issue with an excessive arm motion, while the SIS has no such problem. B) Comparison of the device performance between the SIS (gray) and the commercial one (red), showing an enhanced signal quality from the SIS. Values are normalized to respective baseline idle SNR values. Error bars show standard deviation ($n = 4$). C) Zoomed-in view of raw ECG data measured during an idle state, walking, and jogging, capturing significant motion artifacts from the commercial one compared to the SIS. D) Plots showing a full exercise session with two devices: Normalized ECG waveforms (top), extracted HR and RR (middle), and acceleration data with corresponding activities (bottom). E) Comparison of measured ECG data from the SIS and the Max when a subject has constant arm movements, capturing significant MA from the commercial device.

contact and low impedance. Maximized air permeation of the device on the skin is ideal for minimizing the effect of excessive sweating during the recording session. An SIS incorporates a breathable, long-term wearable, perforated substrate (Figure 5D). The soft elastomeric substrate has an array of stretchable breathing holes, embracing the skin-mounted electrodes. Multi-step molding processes and laser cutting could fabricate an array of 3-mm-tall tapered needles spaced 1.5 mm apart. Perforated breathable substrates were produced by pouring elastomer layers into the epoxy mold. The resulting elastomer substrate has perforations that wick away sweat from the skin to the device's outer surface. Details of the substrate

© 2021 Wiley-VCH GmbH

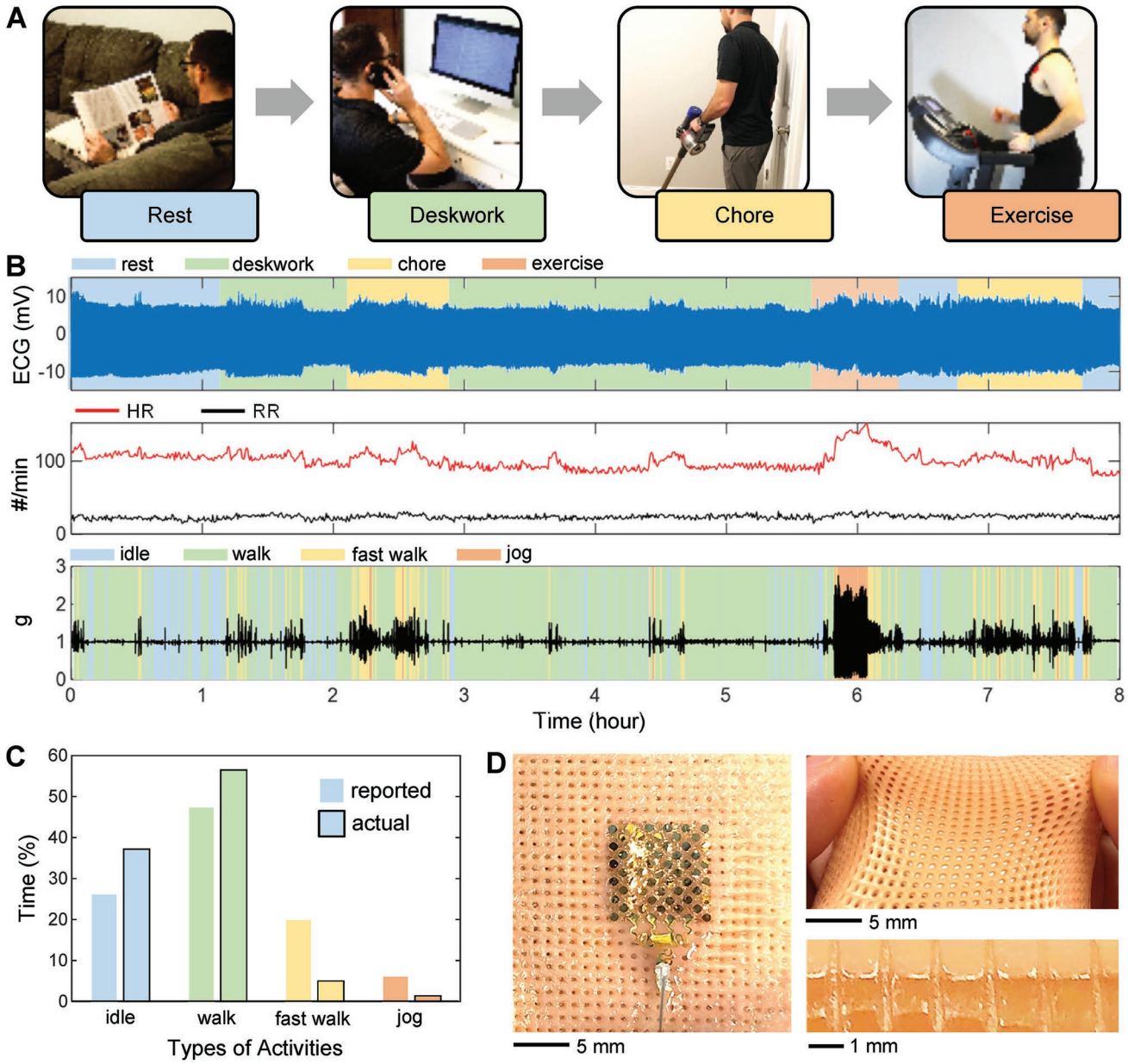

Figure 5. Demonstration of an SIS measuring physiological signals during daily activities for 8 h. A) Representative daily activities (resting, deskwork, chore, and exercise) for increasing motion intensity levels. B) Real-time, continuous recording of physiological data for consecutive 8 h: Raw ECG data with user-reported activities with four different colors (top), measured HR and RR data from ECG, showing clear signals even with excessive motions (middle), and acceleration data with machine learning-enabled classification of four types of activities (idle, walk, fast walk, and jog). C) Normalized percentage difference of total time spent performing each category of four actions (no boundary: User report and black boundary: classified data), showing the sensor's capability to detect accurate activities. D) Photos of a breathable, long-term wearable SIS with a soft perforated substrate, showing an embedded ECG sensor (left), an array of stretchable breathing holes (top-right), and a cross-sectional view of the perforated regions (bottom-right).

fabrication methods appear in Section 4 and Figure S17, Supporting Information. Quantitative air permeation of the developed substrate could be measured by a water vapor transmission test (Figure S18, Supporting Information). The perforated composite substrate (sample #5 in Figure S18E, Supporting Information) shows over ten times higher permeability than the same composite substrate without holes (sample #6). More importantly, additional subjects who wore the SIS show no device lamination issues, excessive sweating, signal degradation (Figure S19, Supporting Information), or skin irritation (Figure S20, Supporting Information), proving the enhanced breathability for consecutive data recording during various daily activities. Overall, the SIS shows a unique performance in strain reduction and real-world applicable continuous recording of health data, compared to the existing wearable ECG monitoring systems (Table 1).

© 2021 Wiley-VCH GmbH

3. Conclusion

This paper collectively reports a new class of strain-isolation physics, hard-soft material integration, and integrated system packaging, enabling an integrated, wireless, long-term usable health monitor. The collected set of analytical, computational, and experimental studies illustrates the first demonstration of a wireless, wearable ECG electronic system that can physically restrict excessive MA during real-life, continuous daily activities without losing data. The presented SIS uses a breathable soft membrane's natural adhesion to offer a skin-friendly, comfortable, continuous recording of ECG, HR, and RR on the skin and real-time classification of various activities via a machine-learning algorithm. An experimental study that compares physiological signal monitoring with two commercial wireless devices shows the exceptional performance of the SIS that maintains the conformal skin contact, enhanced comfort, and high-quality data recording with negligible MA effect. In vivo demonstration of the device used in daily activities over 8 h captures the SIS's feasibility as a most realistic ambulatory health monitor, which can find applications in both clinical uses and consumer healthcare technologies. Future studies will focus on further miniaturizing the device's form factor by integrating fan-out wafer-level packaging and developing all-printing fabrication methods. Finally, large-scale clinical studies in cardiology and pediatrics will be conducted to monitor the health status of both inpatients and outpatients continuously.

4. Experimental Section

Fabrication of a Soft Bioelectronic System: Details of the device assembly steps appear in Section S1 and Figure S2, Supporting Information. A strain-isolation layer was attached to an elastomer using an encapsulating layer, taking care not to allow the elastomer to flow over and increase the substrate thickness directly over the electrodes.

Fabrication of a Nanomembrane Electrode: Details of the electrode fabrication and testing appear in Figures S3 and S4, Supporting Information. Standard microfabrication processes, such as, photolithography, etching, physical vapor deposition, spin coating, and vacuum oven curing, were used to construct the thin-film metal/polymer composite electrodes. Completed electrodes were peeled from an elastomer-coated silicon wafer using a water-soluble tape.

Strain Layer Material Characterization: The strain layer was cut from solid sheets of polypropylene. Various lengths of material were cut and subjected to a bending test to determine Young's modulus for accurate modeling of stiffness. For a sheet modeled as a cantilever beam fixed at one end, the deflection from a force at the tip is calculated by[37]:

$$\delta = \frac{PL^3}{3EI} \tag{2}$$

where δ is the deflection at the free end, P is the force, L is the beam length, E is Young's modulus, and I is the moment of inertia of a rectangular beam (Figure S10B, Supporting Information). From this equation, the modulus can be calculated by:

$$E = \left(\frac{P}{\delta}\right)\frac{4L^3}{bh^3} \tag{3}$$

where $\left(\frac{P}{\delta}\right)$ is the measured value from the bending test and determined by a linear least-squares fit of the data. The Young's modulus was averaged over three trials (Figure S9, Supporting Information) using samples of different lengths and slightly different widths. The SIL sheet thickness (h) for all samples is 0.31 mm, along with the base width (b) = 29.35, 28.78, 28.37 mm, and the length (L) = 18.0, 20.7, 23.2 mm.

Strain Layer Optimization: Strain layer geometry was developed based on the given electrode dimensions. Using the calculated modulus above, and principal mechanics equations,[37] the minimum and maximum thickness were derived to minimize in-plane-strain while allowing for expected out-of-plane bending to maintain conformal contact with the skin. First, the elongation value of the middle section (Figure S10A, Supporting Information) was calculated for the sheet modeled as a prismatic beam, given by:

$$\delta = \frac{PL}{EA} \tag{4}$$

where A is the cross-sectional area for a rectangular beam. The two edge portions are modeled as a simply supported beam with point load and maximum deflection in the middle given by:

$$\delta = \frac{PL^3}{48EI} \tag{5}$$

Together, the elongation in the middle section and bending of the edges add up to the total strain inside the perimeter of the SIL. Combining these equations and solving for h results in this equation:

$$h_{\min} = \frac{PL}{2Eb\delta_{\text{allow}}}\left(1 + \frac{L^2}{12b^2}\right) \tag{6}$$

where $h_{\min}$ is the minimum sheet thickness required to keep the elongation below δ_{allow}. Actual values are P = 1 N, L = 21 mm, E = 1.22 GPa, w = 5.5 mm , and δ_{allow} = 0.64 mm based on 2% strain of the inner dimension L. Resulting in $h_{\min}$ = 14.2 μ m.

Next, the bending of the sheet and adhesion forces (Figure S10C, Supporting Information) are modeled as a simply supported beam with distributed load, given by:

$$\delta_{\max} = \frac{5qL^4}{384EI} \tag{7}$$

where $\delta_{\max}$ is the deflection in the center of the beam, q is the distributed adhesion force per length, L is the beam length, E is the Young's Modulus, and I is the moment of inertia for a rectangular beam. To maintain conformal contact with the skin, the adhesion force must be greater than the beam stiffness for a given deflection. The deflection is determined through geometry and a radius of curvature related by:

$$L = 2r\theta, \delta_{\max} = r(1 - cos\theta) \tag{8}$$

Substituting I, $\delta_{\max}$ and solving for h results in

$$h_{\max} = \sqrt[3]{\frac{5qL^4}{32Ebr\left[1 - \cos(L/2r)\right]}} \tag{9}$$

where $h_{\max}$ is the maximum sheet thickness capable of maintaining conformal contact with the skin when bent around a radius of curvature, r. Actual values are q = 18.32 N/m based on adhesion testing with silbione, L = 32 mm, E = 1.22 GPa, b = 11 mm, and r = 15 mm. Resulting in $h_{\max}$ = 0.31 mm.

Skin Strain Modeling: A circular electrode and skin are in unstrained steady-state configuration (Figure S8A, Supporting Information) and the skin under biaxial strain (Figure S8B, Supporting Information) with stretch ratios λ_1, λ_2. The area of skin in contact with the electrode remains the same. When the skin experiences strain, the electrode moves with the skin, but remains relatively unstrained. This loading scenario causes a portion of the skin that is initially in contact with the electrode to slide out of contact with the electrode. If the skin strain is held constant, then a new steady-state will be reached at the current skin/electrode interface. One source of MA is caused by the impedance change that occurs when the skin moves relative to the electrode. The sensitivity of the skin/electrode interface was quantified by the change in the area in contact at the skin/electrode interface. The stretch ratio is defined as:

© 2021 Wiley-VCH GmbH

$$\lambda_i = \frac{L+\delta_i}{L} = 1+\varepsilon_i \quad i=1,2 \tag{10}$$

where L is the original length, δ_i is the elongation, and ε_i is the strain. This equation can be rearranged to describe the new length as:

$$\lambda_i L = L+\delta_i \quad i=1,2 \tag{11}$$

From Figure S8B, Supporting Information, it can be shown that the stretch ratios also define the new half lengths:

$$a=\lambda_1 r,\ b=\lambda_2 r \tag{12}$$

The change in area is calculated using the area of an ellipse minus the area of the circular electrode:

$$\delta A = \pi ab - \pi r^2 \tag{13}$$

Substituting a, b results in

$$\delta A = \pi r^2(\lambda_1\lambda_2 - 1) \tag{14}$$

Mesh electrodes (Figure S8C, Supporting Information) can be modeled as an N numbered array of small electrodes with a radius r_1, having a total area equal to a single electrode with a radius r_2, the relationship given by:

$$A = \pi N r_1^2 = \pi r_2^2 \tag{15}$$

Therefore, the total change in area is shown below to be directly proportional to the strain, regardless of individual radius, for a given total electrode area by:

$$\delta A = A(\lambda_1\lambda_2 - 1) = \pi N r_1^2(\lambda_1\lambda_2 - 1) = \pi r_2^2(\lambda_1\lambda_2 - 1) \tag{16}$$

Finite Element Analysis Modeling Study: Commercial software ABAQUS was used to validate analytical calculations and optimize mechanical performance. The three main components considered were the elastomer substrate, the PCB circuit, and the strain isolation layer. All components were meshed using hexahedral elements: Elastomer (C3D8RH), PCB circuit (C3D8), and strain isolation layer (C3D8R), with 787 total elements and 1876 total nodes. The elastomer substrate was modeled as a hyperelastic Neo-Hooke material with coefficients $D_1 = 10.152$, $C_{10} = 4.8E-02$. The elastic modulus (E) and Poisson's ratio (ν) are $E_{PCB} = 24$ GPa, $\nu_{PCB} = 0.12$, $E_{SIL} = 1.22$ GPa, $\nu_{SIL} = 0.43$.

Fabrication of a Breathable Substrate: A custom mold was fabricated by laser cutting an array of holes in a 3 mm acrylic sheet. A reverse mold was cast using EpoxAcast 670 HT (Smooth-On), producing a needle array of 3 mm tall tapered needles spaced 1.5 mm apart. Epoxy needles with a base diameter less than 0.5 mm were prone to breaking during elastomer removal. Perforated breathable substrates were produced by pouring elastomer layers into the epoxy mold. Since the perforations are shaped by the tapered needles with a larger diameter base, the silbione layer was applied first for a larger diameter hole facing the skin. This encouraged the outward wicking of moisture from the skin. The silbione was spin-coated at 800 rpm for 60 s and allowed to cure for 24 h. Next, Ecoflex 30 was spin-coated at 200 rpm for 30 s and allowed to cure for 5 h. Final perforated substrates were carefully removed from the mold for thin-film integration with the circuit and electrodes using a similar assembly process as smooth substrates. Total substrate thickness was 1.5–2.0 mm, while thinner samples were difficult to remove from the mold without tearing. Details of the design and experimental photos appear in Figure S17, Supporting Information.

Water Vapor Transmission Study: Water vapor transmission tests were conducted following guidelines from ASTM E 96. Glass jars were filled with distilled water and sealed with elastomer substrate samples of varying thickness, material, and perforation patterns. The samples were placed in a temperature-controlled oven and measured for change in mass at regular intervals. The samples were rotated into a new position following each measurement to reduce the possibility of uneven evaporation between samples. Details of the experimental setup and measured data appear in Figure S18, Supporting Information.

Signal to Noise Ratio Calculation for Electrocardiogram: SNR calculation was made by identifying the heartrate peaks using a variation of the Pan-Tompkins algorithm for detecting the QRS complex.[38] A convolutional filter combines the absolute value of the two adjacent peaks from each QRS complex resulting in a relative amplitude used here as the signal. These signal peaks were removed using a high-order median filter (order = 99), leaving the remaining noise. The signal-to-noise ratio was then calculated using $SNR_{dB} = 10\log_{10}\frac{A_{signal}}{A_{noise}}$ as the ratio of the average amplitude of each QRS complex versus the average noise amplitude.

In Vivo Experiment with Human Subjects: The study involved volunteers ages 18 to 40, and the study was conducted by following the approved IRB protocol (#H17212). Prior to the in vivo study, all subjects agreed with the study procedures and provided signed consent forms.

Supporting Information

Supporting Information is available from the Wiley Online Library or from the author.

Acknowledgements

This work was supported by the Center Grant from the Georgia Tech Institute for Electronics and Nanotechnology and the National Science Foundation/the Centers for Disease Control and Prevention (grant NRI-2024742). Electronic devices in this work were fabricated at the Institute for Electronics and Nanotechnology, a member of the National Nanotechnol ogy Coordinated Infrastructure, which is supported by the National Science Foundation (grant ECCS-2025462). J.-W.J. acknowledges support from the National Research Foundation of Korea (NRF-2020M3C1B8A01111568 and NRF-2021R1A2C4001483).

Conflict of Interest

Georgia Tech has a pending patent application related to the work described here.

Data Availability Statement

Data will be shared upon request.

Keywords

hybrid interfacial physics, motion artifact control, soft wearable bioelectronics, strain isolation

Received: April 29, 2021
Revised: May 25, 2021
Published online:

[1] E. J. Benjamin, P. Muntner, A. Alonso, M. S. Bittencourt, C. W. Callaway, A. P. Carson, A. M. Chamberlain, A. R. Chang, S. Cheng, S. R. Das, F. N. Delling, L. Djousse, M. S. V. Elkind, J. F. Ferguson, M. Fornage, L. C. Jordan, S. S. Khan, B. M. Kissela, K. L. Knutson, T. W. Kwan, D. T. Lackland, T. T. Lewis, J. H. Lichtman, C. T. Longenecker, M. S. Loop, P. L. Lutsey, S. S. Martin, K. Matsushita, A. E. Moran, M. E. Mussolino, et al., *Circulation* **2019**, *139*, e56.

 © 2021 Wiley-VCH GmbH

[2] Z. Zhang, I. Silva, D. Wu, J. Zheng, H. Wu, W. Wang, *Med. Biol. Eng. Comput.* **2014**, *52*, 1019.
[3] M. Kirst, B. Glauner, J. Ottenbacher, *Proceedings of the Annual International Conference of the IEEE Engineering in Medicine and Biology Society*, **2011**, pp. 4804–4807.
[4] Y. Liu, M. G. Pecht, *Proceedings of the 28th IEEE EMBS Annual International Conference* **2006**, PP. 6045–6048.
[5] A. Kalra, A. Lowe, *Sens. Actuators, A* **2020**, *301*, 111726.
[6] H. Zhang, J. Zhao, in *Feature Engineering and Computational Intelligence in ECG Monitoring* (Eds: C. Liu, J. Li), Springer, Singapore **2020**, p. 73.
[7] S. C. Lee, S. M. Kim, *J. Med. Devices* **2016**, *10*.
[8] B. Porr, L. Howell, *bioRxiv* **2019**, 1, https://doi.org/10.1101/722397.
[9] MAX-ECG-MONITOR User Guide. **2018**, 15.
[10] P. M. Barrett, R. Komatireddy, S. Haaser, S. Topol, J. Sheard, J. Encinas, A. J. Fought, E. J. Topol, *Am. J. Med.* **2014**, *127*, 95.e11.
[11] R. Rho, M. Vossler, S. Blancher, J. E. Poole, *Am. Heart J.* **2018**, *203*, 109.
[12] I. Nault, P. André, B. Plourde, F. Leclerc, J.-F. Sarrazin, F. Philippon, G. O'hara, F. Molin, C. Steinberg, K. Roy, L. Blier, J. Champagne, *J. Electrocardiol.* **2019**, *53*, 57.
[13] S. Upadhyayula, R. Kasliwal, *J. Clin. Prev. Cardiol.* **2019**, *8*, 173.
[14] J. A. Walsh, E. J. Topol, S. R. Steinhubl, *Circulation* **2014**, *130*, 573.
[15] R. Herbert, J.-H. Kim, Y. Kim, H. Lee, W.-H. Yeo, *Materials* **2018**, *11*, 187.
[16] H.-R. Lim, H. S. Kim, R. Qazi, Y.-T. Kwon, J.-W. Jeong, W.-H. Yeo, *Adv. Mater.* **2020**, *32*, 1901924.
[17] Y. Fu, J. Zhao, Y. Dong, X. Wang, *Sensors* (Basel) **2020**, *20*, 7.
[18] J. Ottenbacher, M. Kirst, L. Jatobá, M. Huflejt, U. Großmann, W. Stork, *Proceedings of the 30th Annual International Conference of the IEEE Engineering in Medicine and Biology Society*, **2008**, pp. 1695–1698.
[19] Y. Chi, T.-P. Jung, G. Cauwenberghs, *IEEE Rev. Biomed. Eng.* **2010**, *3*, 106.
[20] J. Heikenfeld, A. Jajack, J. Rogers, P. Gutruf, L. Tian, T. Pan, R. Li, M. Khine, J. Kim, J. Wang, J. Kim, *Lab Chip* **2018**, *18*, 217.
[21] J.-W. Jeong, W.-H. Yeo, A. Akhtar, J. J. S. Norton, Y.-J. Kwack, S. Li, S.-Y. Jung, Y. Su, W. Lee, J. Xia, H. Cheng, Y. Huang, W.-S. Choi, T. Bretl, J. A. Rogers, *Adv. Mater.* **2013**, *25*, 6839.
[22] Y.-T. Kwon, Y.-S. Kim, S. Kwon, M. Mahmood, H.-R. Lim, S.-W. Park, S.-O. Kang, J. J. Choi, R. Herbert, Y. C. Jang, Y.-H. Choa, W.-H. Yeo, *Nat. Commun.* **2020**, *11*, 3450.
[23] H. Kim, Y.-S. Kim, M. Mahmood, S. Kwon, N. Zavanelli, H. S. Kim, Y. S. Rim, F. Epps, W.-H. Yeo, *Adv. Sci.* **2020**, *7*, 2000810.
[24] L. Tian, B. Zimmerman, A. Akhtar, K. Yu, M. Moore, J. Wu, R. J. Larsen, J. W. Lee, J. Li, Y. Liu, B. Metzger, S. Qu, X. Guo, K. E. Mathewson, J. A. Fan, J. Cornman, M. Fatina, Z. Xie, Y. Ma, J. Zhang, Y. Zhang, F. Dolcos, M. Fabiani, G. Gratton, T. Bretl, L. J. Hargrove, P. V. Braun, Y. Huang, J. A. Rogers, *Nat. Biomed. Eng.* **2019**, *3*, 194.
[25] E. Huigen, A. Peper, C. A. Grimbergen, *Med. Biol. Eng. Comput.* **2002**, *40*, 332.
[26] X. An, G. Stylios, *Materials* **2018**, *11*, 1887.
[27] N. T. Tasneem, S. A. Pullano, C. D. Critello, A. S. Fiorillo, I. Mahbub, *IEEE Sens. J.* **2020**, *20*, 12799.
[28] H. Chung, A. Y. Rwei, A. Hourlier-Fargette, S. Xu, K. Lee, E. C. Dunne, Z. Xie, C. Liu, A. Carlini, D. H. Kim, D. Ryu, E. Kulikova, J. Cao, I. C. Odland, K. B. Fields, B. Hopkins, A. Banks, C. Ogle, D. Grande, J. B. Park, J. Kim, M. Irie, H. Jang, J. Lee, Y. Park, J. Kim, H. H. Jo, H. Hahm, R. Avila, Y. Xu, et al., *Nat. Med.* **2020**, *26*, 418.
[29] H. Chung, B. H. Kim, J. Y. Lee, J. Lee, Z. Xie, E. M. Ibler, K. Lee, A. Banks, J. Jeong, J. Kim, C. Ogle, D. Grande, Y. Yu, H. Jang, P. Assem, D. Ryu, J. W. Kwak, M. Namkoong, J. B. Park, Y. Lee, D. Kim, A. Ryu, J. Jeong, K. You, B. Ji, Z. Liu, Q. Huo, X. Feng, Y. Deng, Y. Xu, et al., *Science* **2019**, *363*, eaau0780.
[30] Y.-S. Kim, M. Mahmood, Y. Lee, N. K. Kim, S. Kwon, R. Herbert, D. Kim, H. C. Cho, W.-H. Yeo, *Adv. Sci.* **2019**, *6*, 1900939.
[31] R. Lin, Y. Li, X. Mao, W. Zhou, R. Liu, *Adv. Mater. Technol.* **2019**, *4*, 1970065.
[32] Y. Liu, L. Tian, M. S. Raj, M. Cotton, Y. Ma, S. Ma, B. Mcgrane, A. V. Pendharkar, N. Dahaleh, L. Olson, H. Luan, O. Block, B. Suleski, Y. Zhou, C. Jayaraman, T. Koski, A. J. Aranyosi, J. A. Wright, A. Jayaraman, Y. Huang, R. Ghaffari, M. Kliot, J. A. Rogers, *npj Digital Med.* **2018**, *1*, 19.
[33] M. Zulqarnain, S. Stanzione, G. Rathinavel, S. Smout, M. Willegems, K. Myny, E. Cantatore, *npj Flexible Electron.* **2020**, *4*, 13.
[34] W. Dong, X. Cheng, T. Xiong, X. Wang, *Biomed. Microdevices* **2019**, *21*, 6.
[35] Y. Li, Y. Luo, S. Nayak, Z. Liu, O. Chichvarina, E. Zamburg, X. Zhang, Y. Liu, C. H. Heng, A. V.-Y. Thean, *Adv. Electron. Mater.* **2019**, *5*, 1800463.
[36] Y.-S. Kim, M. Mahmood, S. Kwon, K. Maher, J. W. Kang, W.-H. Yeo, *IEEE Trans. Biomed. Eng.* **2019**, *67*, 2159.
[37] B. J. Goodno, J. M. Gere, *Mechanics of Materials*, 9th ed., Cengage Learning, Boston **2018**.
[38] W. J. Tompkins, J. Pan, *IEEE Trans. Biomed. Eng.* **1985**, *32*, 230.
[39] E. Fung, M.-R. JÃ¤Rvelin, R. N. Doshi, J. S. Shinbane, S. K. Carlson, L. P. Grazette, P. M. Chang, R. S. Sangha, H. V. Huikuri, N. S. Peters, *Front Physiol.* **2015**, *6*, 149.
[40] D. Berwal, C. R. Vandana, S. Dewan, C. V. Jiji, M. S. Baghini, *IEEE Sens. J.* **2019**, *19*, 12432.

© 2021 Wiley-VCH GmbH